Journal of Building Engineering 95 (2024) 109937

Contents lists available at ScienceDirect

Journal of Building Engineering

journal homepage: www.elsevier.com/locate/jobe

Full length article

Application of a combination of innovative non-destructive measurement techniques for structural, energetic and safety analysis of buildings

Nicole Janotte [a,*], Benedikt Kölsch [a], Eckhard Lüpfert [a], Johannes Pernpeintner [a], Björn Schiricke [a], Jacob Estevam Schmiedt [b], Dirk Baumbach [c], André Choinowski [c], Dennis Dahlke [c], Ines Ernst [c], Magdalena Linkiewicz [c], Adrian Schischmanow [c], Stephan Dill [d], Tobias Karrer [d], Markus Peichl [d], David Heuskin [e]

[a] German Aerospace Center (DLR), Institute of Solar Research, Linder Höhe, 51147 Cologne, Germany
[b] German Aerospace Center (DLR), Institute of Solar Research, Karl-Heinz-Beckurts-Str. 13, 52428 Jülich, Germany
[c] German Aerospace Center (DLR), Institute of Optical Sensor Systems, Rutherfordstr. 2, 12489 Berlin, Germany
[d] German Aerospace Center (DLR), Microwaves and Radar Institute, Münchener Straße 20, 82234 Weßling, Germany
[e] German Aerospace Center (DLR), Institute for the Protection of Maritime Infrastructures, Rathausallee 12, 53757 Sankt Augustin, Germany

ARTICLE INFO

Keywords:
Mobile non-invasive measurement methods
Acoustic beamforming
Tracer gas
Radar
3D-data integration
Air tightness

ABSTRACT

Mapping and investigating the technical, energy, and safety properties of buildings can be effectively accomplished using Building Information Modelling (BIM) tools. However, detailed geometric and structural information, material properties, and complete BIM models are often unavailable for existing buildings. Renovations, conversions, and aging phenomena further complicate the assessment of a building's condition over its lifetime, necessitating (re)surveying efforts. In a collaborative project focused on studying smoke and gas dispersion pathways in buildings, a multidisciplinary team at the German Aerospace Center (DLR) explored the application of innovative mobile and non-invasive measurement methods to characterize existing buildings, surpassing the capabilities of state-of-the-art techniques. This research entailed the development and testing of enhanced acoustic measurements and H_2 tracer gas techniques for leakage detection. Furthermore, a novel radar system was designed to analyse walls for concealed interconnecting structures. All measurement systems and approaches were collectively demonstrated on an existing office building, with the integration and localization of measurement data achieved through an automated process into a unified 3D database. The information obtained from these comprehensive measurements was visualized within a single-building model. By employing these advanced measurement techniques, a more thorough understanding of existing building conditions was achieved, surpassing the limitations of conventional methods. The successful integration and visualization of the acquired information within a unified model provide valuable insights for future renovations, conversions, and safety analyses. This research contributes to bridging the gap between traditional surveying practices and modern, data-driven approaches, enabling more efficient and accurate assessments of existing buildings.

* Corresponding author.
E-mail addresses: nicole.janotte@dlr.de (N. Janotte), Jacob.EstevamSchmiedt@dlr.de (J. Estevam Schmiedt), magdalena.linkiewicz@dlr.de (M. Linkiewicz), markus.peichl@dlr.de (M. Peichl).

https://doi.org/10.1016/j.jobe.2024.109937
Received 6 December 2023; Received in revised form 4 June 2024; Accepted 12 June 2024
Available online 28 June 2024

1. Introduction

The analysis of existing buildings often necessitates investigations into their structural integrity, safety aspects, and energy efficiency. A significant challenge arises from the scarcity of available structural data, coupled with the unknown conditions resulting from renovations, conversions, and aging phenomena. While Building Information Modelling (BIM) or digital twins can address some of these gaps, they remain exceptional rather than standard practice. To bridge this information gap, systematic surveys of buildings are required. Considering the extensive measurement volumes, overall surveying costs, broad applicability, and acceptance, it is imperative to develop innovative approaches that are efficient, mobile, non-invasive, environmentally friendly, and minimally disruptive to building occupants.

This study focuses on determining the actual geometry of existing buildings and localizing measurement results of novel assessment techniques. This approach ensures that information is not only clearly allocated but can be used to augment BIM with metadata such as airtightness, construction features, and heat transfer properties. However, generating a full building model of the surveyed building was beyond the scope of this study. The required procedure, along with a systematic review and performance assessment of the (automated) generation of digital models from geometric survey data of existing buildings, particularly focusing on object recognition, is detailed in previous work [1,2]. Additionally, a critical review of developments in semantic enrichment with a focus on building and city information models is given in [3].

The motivation to investigate properties of airtightness, gas dispersion, and hidden connection structures is driven by the endeavour to increase energy efficiency, safety in hazardous situations, and general comfort in buildings. Building airtightness is crucial for minimizing uncontrolled air infiltration, which can drastically affect the energy performance. For instance, research in Spain indicates that air infiltration can account for heating demands ranging from 2.43 to 19.07 $\mathrm{kW\,h/m^2}$ per year, depending on the climate zone, with higher impacts observed in continental climates such as Madrid [4]. Similarly, other studies emphasize the influence of air leakage on a building's overall energy consumption, necessitating stringent airtightness measures as part of energy performance calculations [5].

This research also addresses severe health concerns associated with the distribution and dispersion of pollutants in building environments [6]. Studies on dense gas dispersion highlight the significant impact hazardous material releases can have on building occupants and nearby populations. Dense gases, being heavier than air, tend to remain ground-based, leading to slower dispersion and greater hazard ranges, particularly in the presence of obstacles and complex terrain [7]. Additionally, research on airborne transmission of diseases within buildings underscores the critical nature of controlling air movement to prevent the spread of pathogens [8]. High-rise hospitals, due to their structural complexity, are particularly vulnerable to the stack effect, which can facilitate vertical and horizontal transmission of airborne pathogens through HVAC systems [9]. Thus, this study aims to predict and visualize the dispersion paths and potential concentrations of smoke and other harmful gaseous substances using digital twins or BIM.

The following information is of particular interest for achieving these objectives:

- Precise geometry: Serving as the foundation for calculating reference metrics (e.g., distances, areas, and volumes) and georeferencing observations or anomalies.
- Building envelope air tightness: Identifying locations and sizes of leakages/interconnections between rooms.
- Thermal bridges: Recognizing the existence and location of thermal bridges within the building structure.
- Wall structure and shaft locations: Understanding the composition of walls and identifying the location of shafts

This study aims to contribute to the realization of an efficient, mobile, automated, and integrated measurement system that generates digital twins of existing buildings. The findings of this research are anticipated to have practical implications in various fields, including fire protection and smoke extraction, infection prevention, emergency plans in buildings with laboratories, and energy-oriented assessments of existing buildings and their refurbishment. To enable measurements even in areas that may be unsafe for human access due to structural issues or fires, a commercially available automatic and autonomous robotic transportation system such is being explored.

In conclusion, this study introduces a novel integrated measurement system that leverages automation and digital twin technologies to enhance the precision and efficiency of building surveys. Distinguishing itself from traditional approaches, this research utilizes a combination of advanced measurement techniques – including thermal imaging, acoustic transmission analysis, and radar measurements – integrated through an autonomous robotic platform. The core innovation lies in the holistic application of these technologies to not only capture and visualize the physical and thermal properties of buildings but also to model the dispersion of smoke and hazardous gases. This approach aims to provide critical insights for fire safety, pollution control, emergency planning, and energy efficiency assessments, particularly in complex buildings where manual surveys pose significant challenges.

2. Approach

2.1. Test site

To test and demonstrate the efficacy of the new measurement technologies and their integration, a section of an existing office building was selected as the test site. The original construction of the building dates back to 1976, and over the years, it has undergone multiple renovations and adaptations for different uses. Unfortunately, the documentation pertaining to these modifications is scarce, and there is no digital record of the building's structural components, wall structures, or materials used.

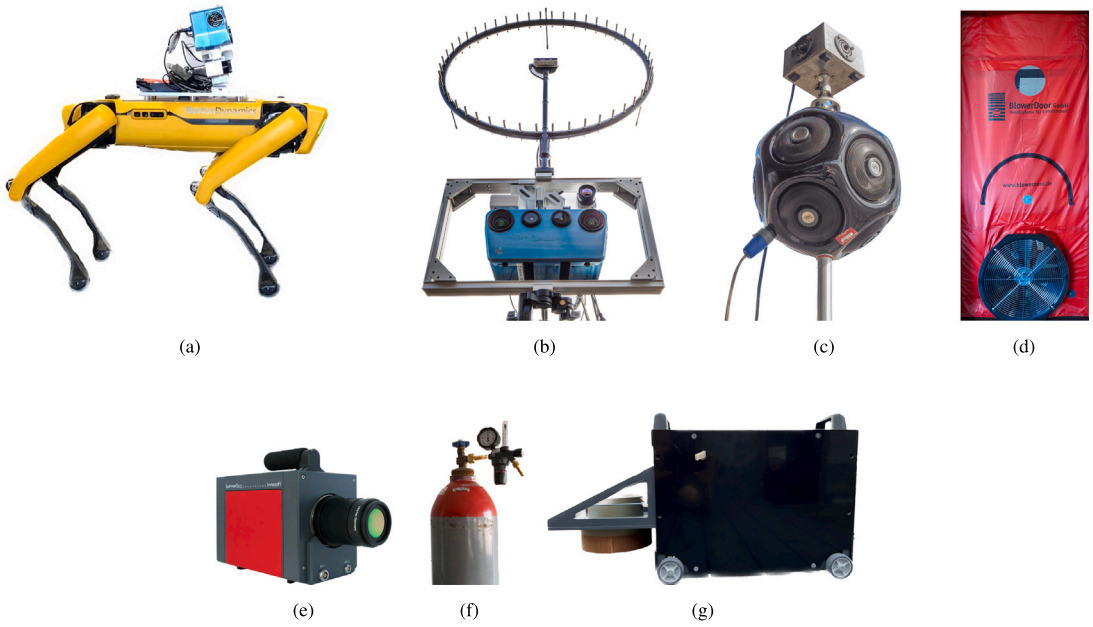

Fig. 1. Overview of devices employed for non destructive analysis of an existing building in this study: (a) DLR's Integrated Positioning System (IPS) mounted on the commercial robot SPOT, (b) Commercial acoustic camera attached to IPS, (c) Commercial omnidirectional speaker, (d) Commercial Blower Door system, (e) Infrared camera, (f) Tracer gas and gas detector (not depicted), (g) DLR's TragRad mobile radar system.

2.2. Employed measurement techniques

In order to assess their capabilities for gathering essential building information, several innovative non-destructive measurement techniques were investigated. The contributions of these techniques to the development of an integrated measurement system are summarized in Fig. 1. The following techniques were employed:

- Commercial quadruped robotic system (SPOT): Utilized as an autonomous sensor carrier platform (Fig. 1(a)).
- 3D scanning: Inner building and room geometry were captured using DLR's camera-based Integrated Positioning System (IPS). This data was used to generate a comprehensive 3D model and spatially reference the inspection measurements (Figs. 1(a) and 1(b)).
- Detection of openings and leakages: Acoustic beam forming and lock-in infrared thermography techniques were employed, in conjunction with cycling pressurization using a blower door, to identify and locate openings and leakages (Figs. 1(b) to 1(e)).
- Gas exchange and air exchange rate measurement: Acoustic measurements and tracer gas techniques were employed to detect gas exchange and measure air exchange rates (Fig. 1(f)).
- Detection of hidden wall structures: Radar and radiometry were utilized to identify concealed wall structures such as hollows, ducts, and funnels (Fig. 1(g)).

For the sake of achieving as comprehensive a demonstration and building analysis as possible, all the measurement techniques described above are combined in this study. In practice, however, individual measurement techniques or combinations thereof would be chosen according to the characteristics of interest. In any case, the clear and quality-assuring localization of the measured locally resolved characteristics requires a system like IPS linking findings to the building geometry. Only global room or building parameters in small units could also be recorded referencing them manually. A robotic transport system is only necessary if a high degree of automation is required or if access to the building is difficult or dangerous.

2.3. Requirements for data/sensor integration

For a seamless integration of all the recorded data into a digital twin, it is imperative to establish unambiguous spatial and temporal associations. This was accomplished through two approaches implemented in this study. The first approach involved a rigid coupling of the Integrated Positioning System (IPS) with the respective measuring system including a geometric calibration. The second approach involved recording the data in relation to measured geometric markers. Both approaches were employed to ensure accurate spatial and temporal alignment of the collected data.

3. Individual measurement/evaluation techniques and their contributions

3.1. SPOT for transport and navigation

SPOT, a commercial terrestrial robot designed for civilian applications by Boston Dynamics, offers unique capabilities for transportation and navigation. Unlike traditional ground drones, SPOT utilizes four legs driven by electrical motors, enabling it to traverse rough terrain, climb steps, and negotiate ledges with a height of up to 300 mm. To aid in obstacle avoidance and spatial orientation, the robot is equipped with stereo camera systems and projects near-infrared patterns for distance determination. Additionally, SPOT features a universal rail system on its top, allowing for the attachment of various payloads. The integration of in-house prototype sensors is facilitated by providing power supply and network communication, enabling the transmission of sensor data via SPOT's wireless network connection. With a maximum payload capacity of 14 kg, SPOT can transport a wide range of equipment or payloads, while achieving a maximum speed of $1.6\,\mathrm{m\,s^{-1}}$.

One of the key advantages of SPOT is its ability to navigate through stairwells, setting it apart from most available drones. This capability makes it ideal for comprehensive mapping of buildings and infrastructures. SPOT can precisely move the sensors it carries on its back at a predefined speed and constant height along a preprogrammed route. This ensures the repeatability and comparability of measurement results, which is crucial when using camera-based, three-dimensional surveying equipment. Unlike multicopters, SPOT's locomotion does not introduce air turbulences that can affect the measurement process of gas detection systems.

SPOT finds valuable applications in repetitive monitoring, cartography, and industrial plant inspections. It excels in providing surveillance and reconnaissance in areas where operator accessibility may be limited or pose significant risks. The robot's ability to implement and validate self-developed prototypes for multi-sensory data acquisition in the field opens new avenues for safety, security applications, and research, yielding previously unattainable knowledge. In the context of this study, SPOT was used to transport the IPS and tracer gas sensor along defined routes during the survey.

3.2. Integrated Positioning System (IPS)

3D scanning with laser and camera systems is a state-of-the-art approach for many applications. In recent years they became popular for digital twin and BIM generation. Integrated sensors provide additional information, such as referenced inspection images, point clouds and others. Commercial systems focus on particular sensing aspects and are thereby limited in their inspection capabilities. An adequate multi-sensor data integrating technology, proposed by Börner et al. [10], can provide a spatio-temporal reference for diverse inspection sensor data. This portable multi-sensor Integrated Positioning System is a real-time technology self-localization and 3D modelling developed at the German Aerospace Center. The IPS performs visual-aided inertial navigation and also has 3D modelling and thermal mapping capabilities [10–12]. Any further kind of inspection sensor data can be given a spatio-temporal reference via the IPS. Therefore, it serves as a basis for spatio-temporal reference for all the inspection sensor data used within the presented experiments. For a typical indoor scenario, IPS achieves a 3D error of 0.1% of the recorded path. All technical data of the device can be found in [10].

3.2.1. Experimental set-up and conduction of measurements

Description of the IPS set-ups

For the measurements, a thermal camera, an acoustic camera and a gas sensor (see Fig. 1) were coupled with IPS and experiments were made on different carrier platforms (SPOT, tripod and handheld). 53 measurements within a week, with and without moving, were done. Particular IPS runs had a duration between 10 and 30 min. Table 1 gives an overview of sensor systems and carrier platform combinations with which the experiments were completed.

Test site preparation

Before starting with the experiments, optical markers (in this case, April Tags) were placed outside the building on both terraces on the ground for geo-referencing the sensor data as well as inside the inspected building floor and offices. The outside marker's geo-coordinates on the terraces were received using a differential GPS survey.

IPS handheld experiments

For generating an overall 3D model of the test site, the IPS was carried manually in several runs over the scene. Starting outside and seeing April Tags on one terrace, IPS was moved inside, through the floor and particular office rooms and recorded sensor data. After finishing sensing the indoor area, IPS was carried to the second terrace to the placed outside April Tags and then through the floor to the starting point on the first terrace back again. This closed-loop approach allows an ad-hoc in-field evaluation of the IPS navigation results quality.

IPS on SPOT set-up and experiments

The ambition to combine both systems (see Fig. 1(a)) was given using SPOT as a platform for autonomous survey and inspection. The IPS battery pack was also fixed on SPOT, just like the operator's laptop. A synchronization of the systems was not necessary. SPOT was first trained and then was able to move autonomously for some experiments. The distance measurement of SPOT uses multiple infrared dot matrix projectors, e.g. for the collision avoidance system. This projection produces a non-natural texturing of the surrounding area, which could negatively affect the IPS navigation algorithm. For this reason, the projectors were disabled.

IPS with acoustic camera setup and experiments

IPS and the acoustic camera were mounted on a tripod on-site (Fig. 1(b)). The set-up is mechanically stable, so the necessary pixel co-registration, allowing subsequent spatial referencing of the acoustic camera data into the 3D model generated by IPS, is

Table 1
Set-ups with IPS participation.

	IPS with thermal infrared camera	IPS with acoustic camera	IPS with tracer gas sensor
SPOT/mobile	X		X
Handheld/mobile	X		X
Tripod/static		X	

(a) (b) (c)

Fig. 2. Exemplary image triplets for extrinsic and intrinsic camera calibration: (a) IPS Left image; (b) IPS Right image; (c) acoustic camera image.

possible. During the acoustic experiments, IPS took one stereo image pair of the scene while the acoustic camera recorded data for a few seconds. The set-up was not moved during the measurements. Several acoustic experiments for leakage detection (see Section 3.3) were done on windows, terrace and office doors with the acoustic camera/IPS outside (see Fig. 6(a)) and a white noise acoustic source (see Fig. 6(b)) inside and vice versa on different positions.

In-field geometrical camera calibration

Accurate geometrical calibration and pixel co-registration of the imaging sensors are necessary for texturing the 3D floor model (generated with IPS) with spectral thermal infrared (TIR) and acoustic data. Therefore, IPS's stereo camera with its thermal infrared camera as well as the IPS's stereo camera with the acoustic visual sensor (see Section 3.3.2) were calibrated and pixel co-registered by chessboard [13,14], either before or after the actual experiments by an appropriate method. Therefore, several image triplets (Fig. 2) of the chessboard target were captured and the calibration parameters were determined.

3.2.2. 3D model

The IPS, in its basic sensor configuration (stereo cameras + inertial measurement unit), estimates a trajectory related to its own starting point. This relative trajectory, shown as the blue line in Fig. 3, is further optimized using April Tags [15], previously placed inside and outside the building. These fiducial markers are detected [16] in both camera images, triangulated and added together with the IPS poses to a landmark simultaneous localization and mapping (SLAM) algorithm [17]. Thereafter, the optimized relative trajectory is transformed into a global coordinate system using five external, georeferenced AprilTags and a seven-parameter static transformation.

In addition to estimating a high-accuracy trajectory with six degrees of freedom, the IPS stereo image pairs are also used to compute high-density depth map sequences. Therefore, graphics processing unit supported image rectification with intrinsic and extrinsic optical camera parameters, which are determined in the preparatory calibration step, and a semi-global matching algorithm (SGM) [18] with a census cost function as described in [19] is applied to the data in this highly computational step. The necessary frame rate of depth maps and local 3D point clouds for the subsequent aggregation of a sufficiently dense global 3D point cloud set is adjusted based on the IPS navigation solution as described in [12]. Cloud and voxel filtering steps based on the Point Cloud Library [20] are applied to all aggregated partial point clouds for the observed area. Fig. 3 shows an overview of the IPS trajectory and the generated 3D point cloud for a base data set of the described measurement campaign. The points are filtered to a 1 cm voxel grid, and the acoustic data are projected to it in the following. All 3D point cloud figures presented in this section are rendered with CloudCompare [21].

The resulting high-resolution 3D point cloud is semiautomatically filtered and then projected onto the XY plane subdivided by a regular grid (compare [22]). For each grid cell, the voxel density and spatial distribution are computed and evaluated to identify potential façade pieces (Fig. 4(a)). On the set of cell elements that are considered as a part of the façade, a regression line is estimated. Then the computation of the regression line is extended to groups of adjacent cells to form façade fragments of the same orientation. For this purpose, the line direction of every cell in a local 8-neighbourhood is pair-wisely compared against the line direction of its centre element using a fixed angular threshold. If the directions match, the respective cells are added to the same cell set. This growth process repeats until no more adjacent cells are left to be assigned. If a stable state is reached, a standard regression line is estimated through the point set of every cell group. The resulting linear façade fragments intersect if their endpoints are locally adjacent (Fig. 4(b)) within the grid, forming a closed topologically correct two-dimensional contour. Finally, the contour is extruded and the floor and ceiling are added (Fig. 4(c)).

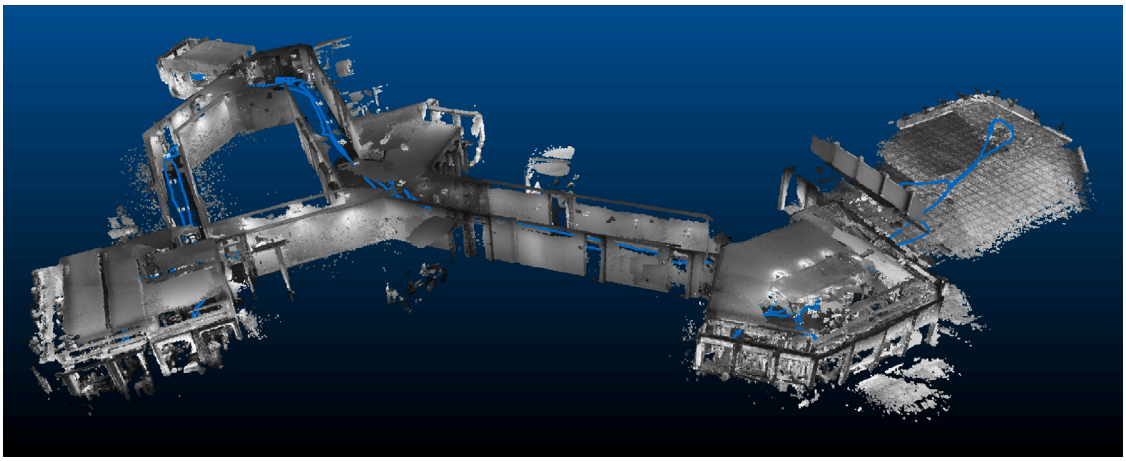

Fig. 3. IPS measurement result of the building section in form of a and 3D point cloud with 1 cm voxel resolution including the IPS trajectory (blue line). (For interpretation of the references to colour in this figure legend, the reader is referred to the web version of this article.)

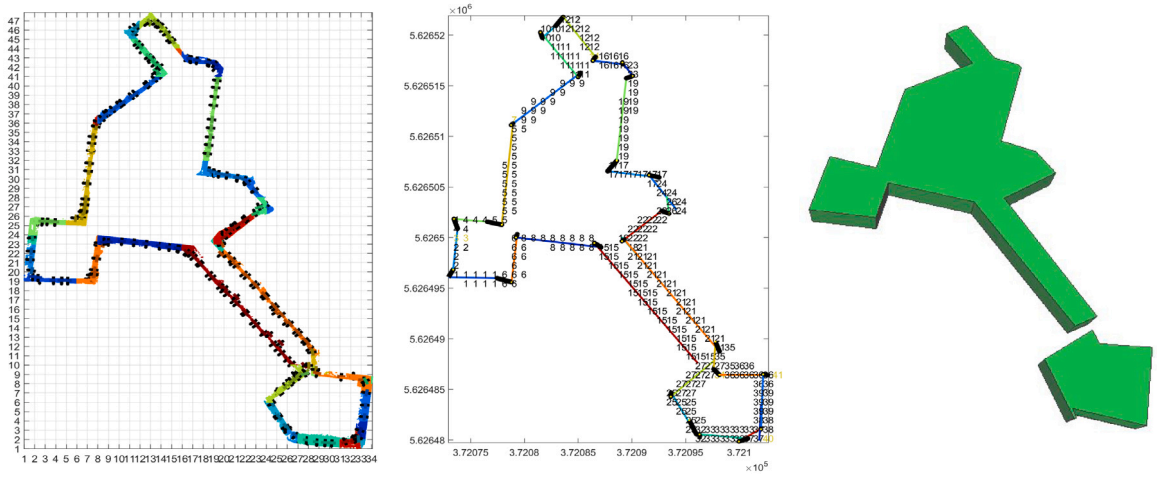

(a) (b) (c)

Fig. 4. Successive steps of 3D vector model reconstruction of the investigated (part of the) floor of the building: (a) point cloud projected onto 2D grid and segmentation; (b) calculated segments and adjacent endpoints of the segments; (c) 3D vector model. Individual segments in (a,b) are identified by randomly chosen colours. (For interpretation of the references to colour in this figure legend, the reader is referred to the web version of this article.)

3.2.3. Results and interpretation

Due to the strong influence of the visual component on the navigation algorithm, the quality of the estimated IPS poses is decisively determined by the feature distribution in the scene captured by the cameras. But if global navigation satellite system (GNSS) or similar is available in the outer areas, the accuracy of these external measurements represents the maximum of the achievable trajectory quality. While the overall accuracy of the 3D model is highly dependent on the accuracy of the generated trajectory, the quality of the point cloud in detail is strongly influenced by the stereo camera parameters, in particular, the pixel resolution and the base length. As shown in Fig. 3, a complete and dense point cloud of 83.3 million points was calculated. The dispersion of the wall points of the projected cloud is only 5 cm (see Fig. 5(a)), which is a good precondition for the 3D vector model reconstruction [23]. The absolute XY position of the point cloud is checked with a reference map by ESRI (Environmental Systems Research Institute, Inc.) and fits the location of the building in the map as shown in Fig. 5(c). The relative accuracy is checked for a few prominent lengths (Fig. 5(b)). On average, target and actual values differ by 0.04 m as presented in Table 2. The average ellipsoidal height of the 3D point cloud is 125 m. If this height is corrected with the value of the geoid undulation of 47 m given by the German Federal Agency for Cartography and Geodesy and with the estimated height of the measurements above ground (fourth floor, approx. 15 m), one gets 63 m. This in turn, corresponds to the elevation above the sea level given in Google Earth.

The accuracy of the 3D vector model is as good as that of the 3D point cloud. However, the calculated vector model shows minor deviations from the point cloud at two places. First, a room was reconstructed separately from the model. In addition, a non-existent

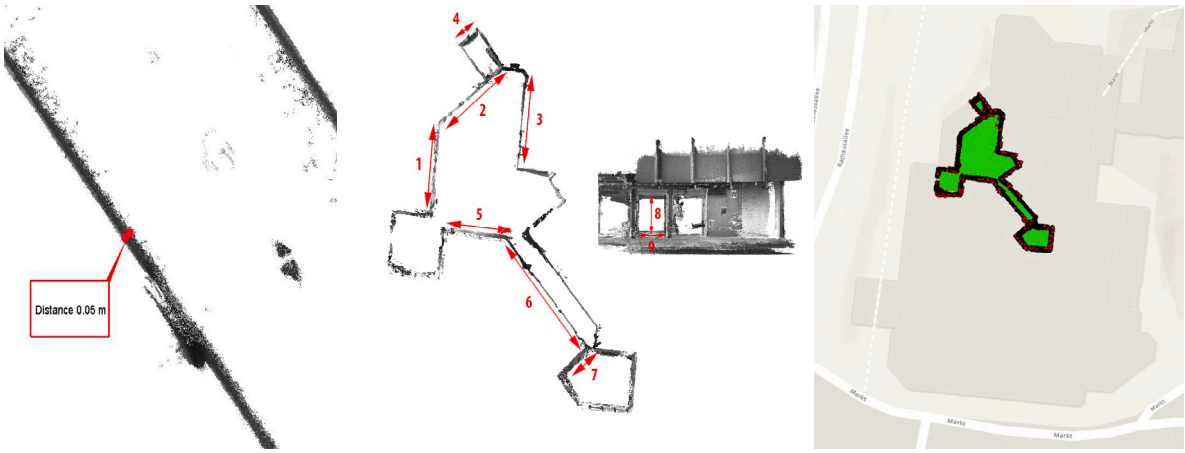

(a) (b) (c)

Fig. 5. Accuracy of the 3D cloud model: (a) dispersion of points of the projected cloud (detail, floor) (b) measured distances to check relative accuracy; (c) absolute accuracy of the 3d cloud model (red–black dots) and of the 3d vector model (green) (reference map: ArcGIS Pro 3.0.0 by Esri). (For interpretation of the references to colour in this figure legend, the reader is referred to the web version of this article.)

Table 2
Selected distances measured in the IPS point cloud (see Fig. 5(b)) compared to the reference distances measured on site for verification of the accuracy of the measured point cloud.

Measured distances (Fig. 5(b))	Target [m]	Actual [m]	Deviation [m]
1	11.39	11.40	0.01
2	9.97	9.94	0.03
3	10.43	10.26	0.14
4	2.75	2.73	0.02
5	9.18	9.26	0.08
6	15.54	15.59	0.05
7	4.89	4.92	0.03
8	2.05	2.07	0.02
9	1.23	1.22	0.01
Average	–	–	0.04

corner was calculated on one wall in this room. It is due to the algorithm, which cannot reconstruct very fine structures. Also, the reconstruction of incomplete parts of the 3D cloud can be problematic for the algorithm sometimes. The absolute accuracy of the XY position is checked in ArcGIS Pro 3.0.0 by Esri and shown in Fig. 5(c). The determined building geometry and location forms the basis for the localization of all further measurement data.

3.3. Acoustic leakage detection

3.3.1. State of the art

Assessing the airtightness of buildings is integral for understanding its overall performance, as it directly influences aspects such as energy efficiency [24–26], indoor air quality [27], thermal comfort, or structural safety. The objective of the acoustic measurements proposed in this paper is to identify small openings in building enclosures for these reasons and to detect potential gas propagation pathways within buildings. This knowledge of leak locations enables prioritized sealing of more significant leaks and improves estimates of infiltration airflows [28].

To date, acoustic methods have been rarely utilized in building airtightness analysis. One possible approach was suggested by the ASTM E1186 standard [29], and previous work by Keast et al. in the 1970s [30]. Several studies have examined sound transmission through walls in laboratory settings [31–36] and field tests [37–40] to quantify leaks, yielding some successful results.

3.3.2. Measurement set-up and conduction of measurements

This paper introduces an acoustic beamforming method utilizing a microphone array, often referred to as an “acoustic camera”, to detect and visualize sound sources. Beamforming is a signal processing technique that allows for the distinction of sound sources from different directions using the microphone array. The advantage of employing an acoustic camera for various applications is the visual output, which can be overlaid with a visible image of the same scene. For a detailed understanding of the operating principle of the acoustic camera, see Refs. [41–45].

(a) Microphone array outside the building with integrated IPS

(b) Omnidirectional setup with a high-frequency (top), a mid/low-frequency (bottom) speaker inside the building

Fig. 6. Measurement setup for beamforming measurement of the building façade outside the building and measurement setup of a high-frequency (top), a mid/low-frequency (bottom) omnidirectional dodecahedron speaker inside the building.

(a) Existing leak in the window

(b) Constructed leaks in the window

Fig. 7. Location and nature of window leaks in the examined using beamforming and lock-in thermography.

In the measurements conducted for this paper, the "Acoustic Camera Array Ring48 AC Pro" from the company gfai tech GmbH was used. It has 48 equally spaced microphones and a diameter of 0.75 m (see Fig. 6(a)). The recommended frequency range for this array lies between 164 Hz and 20 kHz, although localization of higher frequencies (up to 60 kHz) is possible. In this case, all microphone signals were sampled at a frequency of 192 kHz and digitized with 32 bit. An optical camera (resolution: 1920 × 1080 pixels) was positioned at the centre of the array to capture a visual image of the measured scene.

The acoustic camera was placed on one side of the wall, while a pair of speakers were positioned on the other side. For this measurement campaign, a high-frequency speaker with a frequency range of 15 to 120 kHz and a mid/low-frequency dodecahedron speaker with a range of 0.05 to 16 kHz were used (see Fig. 6(b)). To measure the building envelope, the acoustic camera was positioned outside, while the speakers were placed in the centre of the room. Throughout the measurements, the acoustic camera and speakers remained stationary. The sound waves produced by speakers penetrate through the leaks in the wall and can be detected as individual sound sources on the other side of the wall by the acoustic camera. A computer-generated broad-band white noise signal with a level 85 dB was emitted inside the building for a duration of 6 s.

In addition to visible pre-existing leaks in the window frame (Fig. 7(a)), plastic stripes were intentionally placed at two points into the window gasket to create artificial and reproducible leaks for detection (Fig. 7(b)). For enhanced visualization in the 3D model, this system was calibrated and integrated with the IPS as described in Section 3.2.1.

3.3.3. Results and interpretation

Figs. 17(a), 17(c) and 17(e) present optical camera images of the examined window façade with selected superimposed results from the beamforming analysis conducted by the acoustic camera, recorded from the white noise generated inside the building.

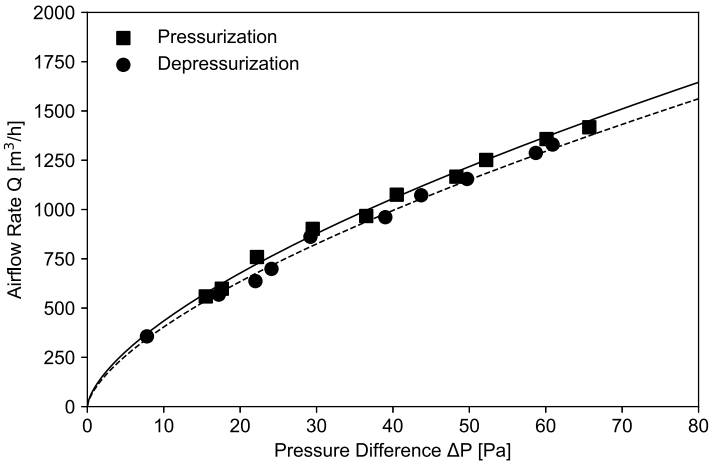

Fig. 8. Linear display of pressurized and depressurized blower-door measurements of the meeting room.

These figures display selected third-octave frequency bands with centre frequencies of 1.6 kHz (Fig. 17(a)), 4 kHz (Fig. 17(c)), and 20 kHz (Fig. 17(e)). The colour scale represents the upper 3 dB range of the displayed sound pressure level.

In Figs. 17(a) and 17(c), significant sound sources of up to 40.4 dB are visible in the upper left part of the window frame at a third-octave frequency bands around 1.6 kHz and 4 kHz. These sound sources may correlate to the pre-existing leak shown in Fig. 7(a) and the left-constructed leak using plastic stripes shown in Fig. 7(b). At higher frequencies around 20 kHz, even the tiny leaks at the top and bottom of the inserted larger plastic strips at the left part of the window are visible. The smaller plastic stripes inserted in the right part of the window are not visible. These visualizations of sound sources are later used in combination with the IPS to be visualized on the 3D Model of the building part, see Section 4.1.2.

3.4. Blower door as a measure of building air tightness

3.4.1. State of the art

The blower door test, defined by international standards [46,47], and its uncertainties are investigated in several studies [48,49]. It involves installing a blower in the main door of the building, which induces airflow into or out of the building, measuring the airflow rate Q and the pressure difference ΔP between the inside and outside. The relationship between airflow and pressure difference is commonly described using a power law formulation, as outlined in the standards.

3.4.2. Measurement set-up and conduction of measurements

In this study, one pressurization and another depressurization was conducted in a meeting room using a Minneapolis Blower Door M4 (measuring accuracy of flow rate: ±4% of the reading) according to ISO 9972 [46]. From these tests, the air change rate per hour was deduced by interpolating the airflow at 50 Pa (Q_{50}) and normalizing it by the room's volume V.

Additionally, the blower door was utilized for periodic pressurization in conjunction with the lock-in thermography technique described in Section 3.5.

3.4.3. Results and interpretation

Two series of blower door measurements were conducted in the investigated meeting room, with separate tests for pressurization and depressurization. Fig. 8 presents the measured pressure differences and their corresponding airflow rates. The calculated air change rate per hour at 50 Pa (n_{50}) from the fitted data was found to be 7.62 h^{-1} for depressurization, 7.98 h^{-1} for pressurization, with a mean value of 7.80 h^{-1}. Based on this leakage rate, the room can be classified as significantly leaky, resulting in increased infiltration heat losses.

3.5. Thermography

3.5.1. State of the art

Infrared (IR) thermography is a technique for visualizing surface temperature distributions, crucial for detecting leaks if there is a temperature difference between the air and the surface, the flow is in the appropriate direction, and the camera has a clear line of sight to the surface with temperature variations. Interpreting IR images to identify leaks requires experience to differentiate between effects caused by insulation inhomogeneities, surface emittance, 3D geometry, solar irradiation, wind, or other factors. Integrating a blower door system, as shown in Fig. 1(d), can significantly enhance the effectiveness of thermography, by controlling the direction of airflow through the leak, enabling the use of differential images [50] and change analysis of time series [51].

Lock-in thermography [52], typically employed for component testing, can be adapted for leak detection, when combined with a blower door. Consequently, the benefits of lock-in amplifiers [53], such as noise reduction and suppression of perturbations at frequencies other than the excitation frequency, can be harnessed for leak detection using IR imaging. The process involves cyclic operation of the blower door and applying Fourier transform analysis to IR image sequences to identify the building's response at the excitation frequency, with phase filters mitigating environmental interference effects. Details are described in [54].

In the presented campaign, two IR cameras were used, each with different evaluation methods:

- IPS-integrated IR camera: Images were evaluated as normal evaluation as normal IR images. The integration with IPS facilitated localization and automatic integration into the 3D model. Detailed measurements and results are described in Sections 3.2 and 4.1.1.
- Stand-alone IR camera: Measurement and evaluation were performed using lock-in thermography, which will be discussed in the following section.

3.5.2. Measurement set-up and procedure for lock-in thermography

The measurements were conducted on the façade outside the meeting room, as depicted in Fig. 7, with similar preparations as described in Section 3.3 involving the use of plastic strips to create artificial leaks. The chosen IR camera, InfraTec ImageIR 8380, is sensitive within the range of 2 µm to 5 µm and has a thermal resolution of 25 mK. The emittance is set to 1. This is considered to be sufficient here, as thermography is used as a tool to visualize leaks using the lock-in method. In that context, primarily relative temperature differences in the scene and temperature changes at the frequency of excitation are relevant. By cyclically switching on and off the blower door, a periodic pattern of over-pressure of 75 Pa for 20 s and near-zero over-pressure for another 20 s was generated for three periods. Air temperature of the interior and exterior was measured with thermocouples protected from direct sun light, values for individual measurements are included in Fig. 9(a) and b. The weather conditions during the IR measurements were challenging, with gusty wind, rapidly changing irradiation conditions, and quickly shifting cloud patterns in the sky.

3.5.3. Data processing for lock-in thermography

For each pixel, the complex Fourier Transform is calculated, and the value for the excitation frequency is extracted from the spectrum. This process enables the creation of amplitude and phase images. While the phase image is commonly used in lock-in thermography applications, in this case, the amplitude image is of higher immediate value. In order to further suppress artifacts resulting from the unstable radiation environment, phase and amplitude image are combined by filtering the amplitude image for specific phase. This phase-filtering was achieved by computing the scalar product of the complex Fourier transform and the complex representation of the evaluation vector at the desired phase (cf. [54]). The appropriate phase for evaluation was manually chosen.

3.5.4. Results and interpretation for lock-in thermography

Fig. 9(a) displays an IR image after 30 min operation of the blower door. The central door and the windows on either side are visible. In the foreground, the terrace floor is heated by direct solar irradiation. The circle in the top-left corner is lens flare. Reflections in the door and windows reveal the terrace floor and the guard rails. The plastic strips on the right side of the door exhibit lower radiation temperature, potentially indicating a leak, although this lower temperature could also be attributed to differing surface properties. Interpretation of the image and proper leak detection necessitate additional knowledge about the object and the relevant physics.

Fig. 9(b) shows the result of a lock-in thermography measurement made two hours after the measurement of Fig. 9(a). The phase filter was set manually to 60°. The artificial leaks on both sides are visible. Especially the leak on the plastic strip on left side causes a prolonged leak in the seal in the upper left corner of the door.

A comparison between the results of lock-in thermography Fig. 9(b) and the acoustic measurement Fig. 17 and is noteworthy: while lock-in thermography detected the artificial leak on the right side that the acoustic system missed, the existing leak shown in Fig. 7(a) cannot be seen in Fig. 9(b), although it was detected by the acoustic measurement (cf. Fig. 17(a)). It is possible that the air exits of the leak are simply outside the image boundaries. Alternatively, this disparity could be a physical effect highlighting the limitations of lock-in thermography. As the existing leak leads to the cabinet of the Venetian blind above the door, the air from inside the building passes through the cabinet before exiting to the outside, possibly mixing with the air reservoir inside the cabinet. Additionally, the air passing through the relatively small hole on the inside spreads over a larger area through the Venetian blinds. Consequently, the air may not significantly affect the temperature of the surface observed by the camera. An investigation of absolute detection sensitivity of the method has not been performed in the context of this measurement campaign, as this would have required the quantification of the leaks detected in the images. This is reserved for future work.

3.6. Tracer gas measurements characterizing gas dispersion

3.6.1. State of the art and needs in TragSens

Tracer gas techniques involve adding a small quantity of a tracer gas to air to measure air exchange or leakage rates by tracking the gas's concentration decrease, often using sulphur hexafluoride (SF_6), a strong greenhouse gas, for its absence in natural environments and detectability in low quantities via gas chromatography. Despite its effectiveness, alternatives like syringe sampling for lab analysis offer cost benefits but are slower. Other detection methods include photo-acoustic infrared sensors and electron capture detectors, though they necessitate higher, environmentally impactful SF_6 levels.

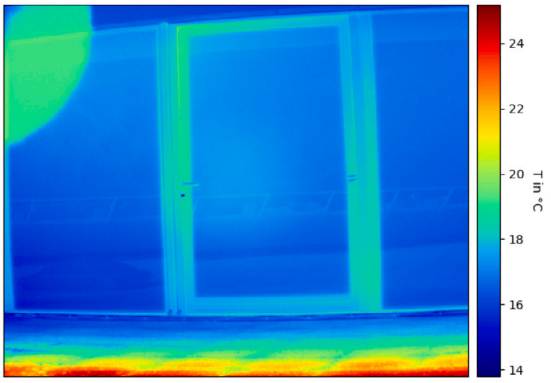

(a) IR-image after 30 min of continuous blower operation at 75 Pa, air temperature 24.5 °C (interior) and 21.5 °C (exterior), mean of 1 min at 60 Hz

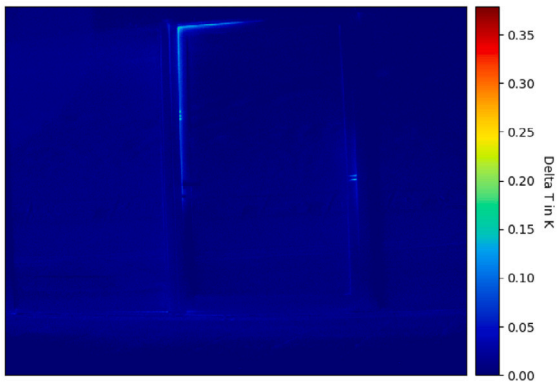

(b) Amplitude image of lock-in thermography with phase filter at 60 °C, air temperature 26.7 °C (interior) and 21.5 °C (exterior)

Fig. 9. Comparison of thermography and lock-in thermography measurements with phase filter of a façade door.

Hydrogen (H_2), with a minimal presence in ambient air, serves as a tracer gas in select applications due to its safe indoor use and environmental benignity. Its application in air exchange rate measurements is uncommon, despite its frequent use in leak detection in pipelines and flat roofs. Laboratory measurements benefit from highly sensitive mass spectrometers, while portable options include semiconductor or photoionization detectors, with infrared technology is unsuitable for hydrogen detection.

Recent studies, such as those by Liu et al. [55] and Mu et al. [56] have investigated airflow and hazardous gas dispersion in buildings using various methods.

3.6.2. Measurement set-up and conduction of measurements

For this study, hydrogen is chosen as the tracer gas due to its cost-effectiveness, environmental friendliness, ease of handling and mobility. The necessary equipment includes portable meters with electronic interface for data reading and devices for metring and distributing the hydrogen in the room. The gas is metred in the room using a pressure reducer with integrated variable area flow meter with a measurement range of 50 L/min and hand valve specially designed for this type of gas. The gas is distributed in the room using a thin hose of 4 mm inner diameter at the pressure reducer and a fan. Semiconductor sensors are primarily used for detection, while thermal conductivity detectors and portable photo-ionization detectors are employed in specific phases. This test used the instrument Sewerin EX-TEC GM4 based on an electrochemical sensor for the hydrogen concentration range 40 .. 4000 ppm and a measurement uncertainty of 10% stated by the manufacturer. In a preceding lab test the linearity of the sensor was successfully cross-checked, which is relevant for the decay curve measurements.

Two different scenarios are distinguished: The **“airport” scenario** simulates the diffusion of a (dangerous) substance from a single source in a large building, like an airport. The substance migrates from high to low concentration areas according to the air exchange rate between such spaces. This phenomenon was studied using hydrogen (as 5% forming gas) as the model substance, using a single sensor periodically recording local hydrogen concentration. In combination with recording of the respective locations, the concentration time series for each location are extracted.

The **“leakage” scenario** is a simpler leakage model involving a single room with an initial concentration of the substance, observing its exponential decay over time due to air exchange with adjacent spaces and the environment.

Both scenarios aim to characterize physical parameters for simulating complex setups based on air exchange rates.

3.6.3. Results and interpretation

In the “airport” scenario the data from room 4.03, as shown in Fig. 10, display a near-linear increase in H_2 concentration within an hour of releasing the contents of one 50 L cylinder of forming gas. A maximum concentration of 2700 ppm is reached. The light-grey curve shows a total of 13 walkarounds with the sensor on a repeated track in defined office space section of the building, see figures in Section 3.2.2. Room 4.03 then exhibits the typical exponential decay. In adjacent rooms, specifically rooms 4.04 and 4.05, there is a noticeable sharp increase in concentration, which then follows an exponential decay. This behaviour suggests that these rooms, being in close proximity to room 4.03, are directly affected by the gas dispersion from the source room.

Room 4.18, being located at the opposite side of the floor, presents a different pattern. The concentration in this room increases at a comparatively slow rate, peaking at a value significantly lower than the source room. The sensor signal from this room does not return to zero concentration within the span of a 4-h measurement campaign. This indicates a prolonged presence of the tracer gas and suggests a varying influence of the source room based on spatial positioning and potential airflow dynamics within the building.

The variations in the rise and decay of concentration across different rooms underscore the complexity of gas dispersion in such a large structure. It becomes evident that a simplistic model, based solely on air exchange rate decay, will not be sufficient to capture

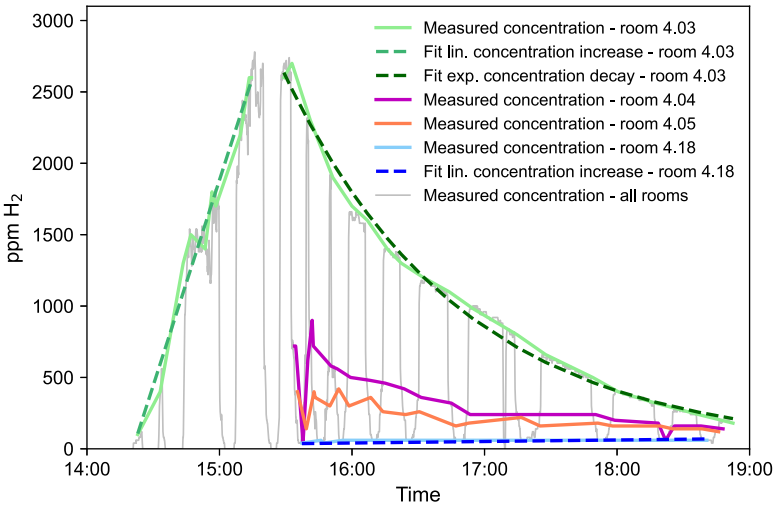

Fig. 10. Complete H_2 concentration measurement series recorded 27-Sep-2021 KAS 4th floor for the "airport scenario".

these intricacies. The need for a more comprehensive model is highlighted, one that considers individual room volume, inter-room airflow, local air exchange rate, and potential barriers to gas movement.

For future studies, it will be beneficial to place multiple sensors in strategic locations within the building to capture a more detailed dispersion pattern. This approach would provide real-time data from various points, offering a more comprehensive view of gas movement. The use of H_2 as a non-hazardous forming gas is advantageous, especially in large, operational buildings. It ensures safety while allowing for real-world measurements without necessitating building evacuation.

3.7. Radar wall structure analysis

3.7.1. State of the art and needs in TragSens

Microwave radar has a long-standing tradition as a valuable tool for detecting concealed objects or structures in various fields such as ground penetrating radar (GPR) for mining, geophysics, archaeology and general ground exploration [57–59], radars for detection of landmines and unexploded ordnance (UXO) [60–62], or systems for the investigation of building fabric like bridges or other large concrete constructions [59,63–66]. However, the use of radar for detailed analysis of fine building structures, including precise wall constructions and the detection and interpretation of unexpected anomalies, remains relatively rare. Therefore, there is a compelling need for a more comprehensive investigation of these phenomena. In a previous project, essential theoretical and experimental work was conducted to determine the number of layers, layer thickness, and layer permittivity of walls [67,68]. This experience serves as the foundation for building and testing a hand-carried radar system and validating its effectiveness on existing buildings.

The objective of radar measurements along building elements, such as walls and ground floors, is to non-destructively and precisely determine their hidden depth structure. Microwaves in the lower frequency domain, below approximately 10 GHz, have the capability to penetrate dielectric materials and exhibit complete reflection by metallic surfaces. Different materials possess distinct permittivity values, which is an electromagnetic property describing the material's electric polarization capability. Variation in permittivity results in different wave impedance, leading to partial reflection of the incident wave at material transition. Consequently, radar can provide information about the range-dependent reflection profiles of a layered medium. By moving the radar along a surface, a two-dimensional image of the reflection behaviour, depicting depth versus along-track direction, can be obtained. These images can then be analysed to reveal sub-surface structures, indicating different material types, layers, thicknesses, inclusions, hollows, or any localized objects of interest. Furthermore, by incorporating prior knowledge and scene modelling, additional parameters such as permittivity, density, and even thermal behaviour can be derived [69].

3.7.2. Measurement setup and conduction of measurements

As part of this cooperation project, the TragRad radar system was specifically developed and constructed to enable flexible and manual operation inside buildings for monitoring the internal structure of walls and ground floors. Fig. 11 (left) shows the TragRad system in operation on an existing office building.

TragRad is designed and constructed as a stepped-frequency radar using the frequency range of 1–4 GHz. Hence a corresponding range or depth resolution in air of about 5 cm can be achieved. Within another medium than air, the depth resolution can improve up to 1–2 cm, depending on the dielectric constant of the material. Due to the close distance to a wall, the lateral spatial resolution is roughly determined by the antenna aperture, being in the order of about 10 cm close to the antenna, and degrades to about 15 cm at a distance of 30 cm to the antenna aperture. Due to the close distance to the interesting scene of a wall structure, measurement errors

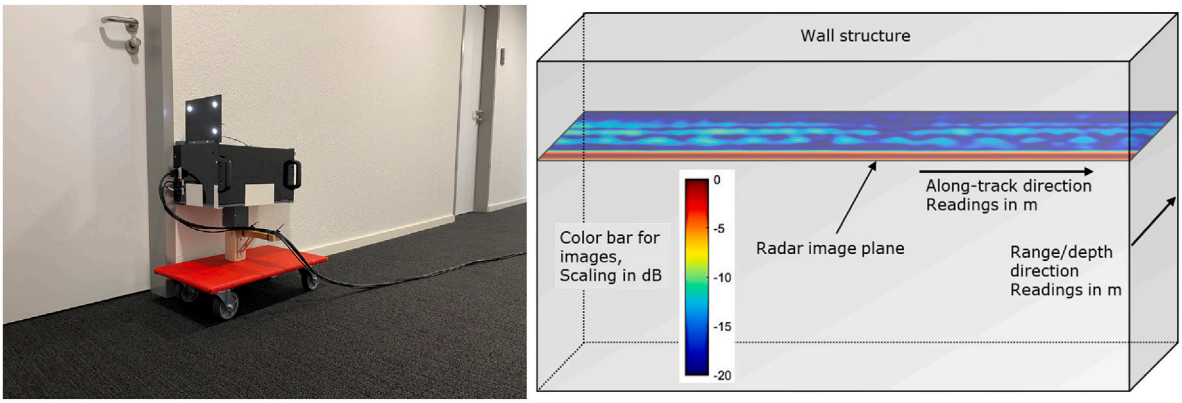

Fig. 11. Left: Photograph of the TragRad radar during operation by scanning a wall. Right: Sketch of a radar image with respect to the scanned wall as produced from data processing. A typical result shows radar reflectivity, i.e. echo intensity, in decibels over driveway and depth, both in metres.

can be neglected and the performance is mainly dictated by the spatial resolution and near-field interaction of the electromagnetic waves with the wall structure itself.

The radar device is supported by a pillar mounted on a small creeper, allowing for easy manual movement along a wall at a constant height above the floor, as defined by the length of the pillar. The radar is equipped with small wheels touching the wall, ensuring a constant distance between the radar antenna and the wall surface. Three LEDs are observed by an optical camera during the measurement to determine position data, forming an optical tracker with an accuracy pretty much higher than the spacial resolution. For ground floor measurements, the radar is simply rolled along the floor surface using its wheels.

3.7.3. Data processing

While moving along the wall or the ground floor, the TragRad radar transmits microwaves within a specific frequency range and receives the corresponding echoes in a very short time. Hence, several frequency profiles are measured in short sequences. To transform the frequency profiles into range profiles, a series of special signal processing techniques, including Fourier transform, are employed. Once the linear wall scan, as depicted in Fig. 11 (right), is completed, all range profiles are arranged based on their distance to the optical tracker. This arrangement results in a two-dimensional radar image, representing the echo or reflection distribution of the wall in both depth and along-track directions. The generated radar image provides valuable information about the internal structure of the wall, allowing for the identification of layers, local objects, and anomalies. The interpretation of the radar image and the extraction of meaningful insights currently rely on manual analysis and expert interpretation.

3.7.4. Results and interpretation

The present study was used to validate the TragRad radar on real objects. The interior wall structures of that building were mainly formed by drywall and concrete constructions, on the one hand for separating office rooms and on the other hand as a truss for the ceilings and lift shafts. For the richness of detail of such measurements, the two-dimensional radar image of one side wall of an inner office corridor is illustrated and discussed. Fig. 12 shows the radar images of selected corridor segments together with a photograph and part of an old building plan.

The corridor has a length of about 10 m. The side walls appear optically identical in fabrication along the whole length. The illustrated side wall is only suspended by a door and an adjacent integrated pillar of glass brick for decoration purposes. The shown photograph is warped in the horizontal direction for better illustration since the photographic perspective of a long corridor results in only a narrow side wall representation. Hence, the pictured TragRad system also appears excessively stretched on the left side. The old building plan shows basic wall construction. Two side walls are visible, separated by the door, partly mapped by the illustrated radar signatures indicated by the orange bars on the plan and the photograph. Besides visual and touching surface inspection, the only further available information was that the wall should be made of drywall construction.

The illustrated radar sections have been selected since they show three different types of wall construction, although they belong to the same side wall of one corridor without any optical peculiarity. Section 1 shows clearly where the outer surface of the drywall starts, being roughly the centre line of the elongated orange strap. Note that due to the finite spatial resolution, only positions of the maximal values of thin radar signature features should be used for position reading. Furthermore, three pillars for fixing the drywall plates can be identified, starting close to the outer surface. Hence, this may indicate a single-layer panelling used for cost reduction. A second strap-like echo in mostly cyan colour shows the inner drywall surface, having most probably identical thickness. In addition, on the right part of the radar image, an additional echo in larger depth indicates the presence of a cross wall which can also be recognized from the plan.

Section 2 shows the presence of a cross wall being validated again by the plan. On the right side of the cross-wall signature, the drywall panelling seems different. While the outer surface appears similar, the pillars now start at a slightly larger depth. This gives rise to the assumption that the second strap-like signature belongs to the end of the outer panelling, indicating larger thickness,

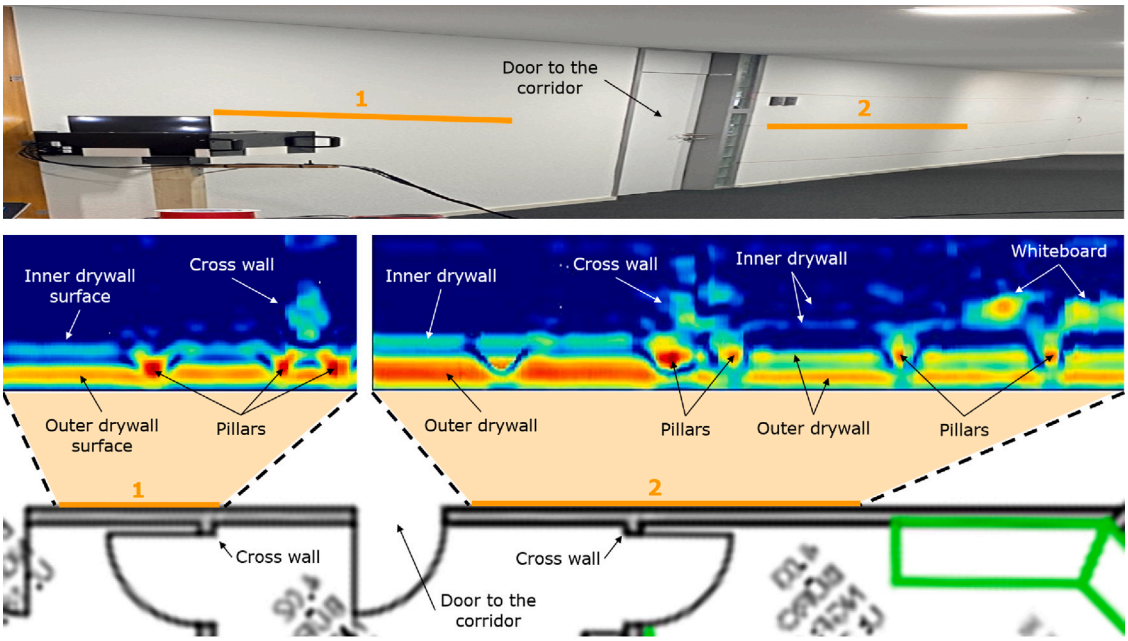

Fig. 12. Example for radar results together with some meta information. Top: Warped photograph of the wall of an office corridor. The orange bars 1 and 2 indicate roughly the areas for which the radar images below are shown. Bottom: Part of an old building plan indicating the basic wall segmentation. The orange bars indicate the illustrated radar tracks again. The plan is mirrored with respect to the photograph for simpler illustration. (For interpretation of the references to colour in this figure legend, the reader is referred to the web version of this article.)

e.g. double-layer panelling. In addition, two further weak signatures behind the pillars can be recognized, indicating the echoes of the inner drywall panel. On the right image part, an additional signature resulting from a whiteboard mounted on the inner wall of the office room can be recognized. The depth locations of the echo maxima are in line with the outer echo of the inner drywall, hence confirming its presence.

Left of the cross-wall area of Section 2, yet another wall construction can be observed. Here, the beginning of the outer drywall cannot be identified as clearly as before since the strap-shaped signature is much broader, indicating another type of panelling or material. The same is valid for the inner drywall signature. The pillar position seems to be similar compared to the right side.

The short analysis presented here impressively shows the power and potential of highly resolved radar signatures for inspecting building structures. Very slight changes in fabrication can be clearly identified. However, the interpretation of radar signatures and their association with true construction details has still to be explored in more depth.

4. Combined results

4.1. Data integration

The processed data of all inspection sensors (thermal infrared, acoustic, lock-in thermography and radar) is integrated via spatio-temporal referencing and then projected onto the IPS 3D vector model, which represents the digital twin. Various methods were used to integrate the data (Table 3). Some data, such as those from thermal imaging or acoustic camera, were co-registered via geometric chessboard calibration. Other data, such as radar and lock-in thermography, were incorporated into the model in the post-processing through spatial referencing via control points. Fig. 13 gives an overview of the workflow and results.

4.1.1. IPS-IR camera

IPS can simultaneously record additional sensor data synchronized with stereo images and IMU data. Figs. 14(a) and 14(b) show a left IPS image and an IR image recorded at the same time. In the case of image data, they can be immediately mapped onto the 3D point cloud, which is used to map the thermal information in colour representation from the additional thermal camera. An exact trifocal geometrical calibration, as described in [14], is mandatory here.

By projecting the local 3D points into the valid IR camera image, considering the internal and relative orientations, the colour or measured temperature values can be assigned directly to the respective surface points. A voxel-based occlusion algorithm prevents incorrect colour assignments on occluded 3D points. They could be caused by the different points of view of the left stereo and the IR camera. In a subsequent automatic filter process, voxels and their additional information are removed based on the number of 3D points found per voxel, the proportion of values with additional information and their reliability. The final 3D object view

Table 3
Data integration methods applied for localization of measurements and results in this study.

Sensor	Spatio-temporal reference
IPS-Thermal	Automatic IPS and thermal infrared camera synchronization, automatic pixel co-registration via geometric chessboard calibration, automatic trajectory spatial referencing on optical markers in global coordinates
Acoustic camera	Automatic pixel co-registration between IPS and acoustic camera via geometric chessboard calibration, manual spatial referencing via point cloud features
Lock-in thermography	Manual spatial referencing via point cloud features
Tracer gas	Timestamp
Radar	Manual spatial referencing via point cloud features

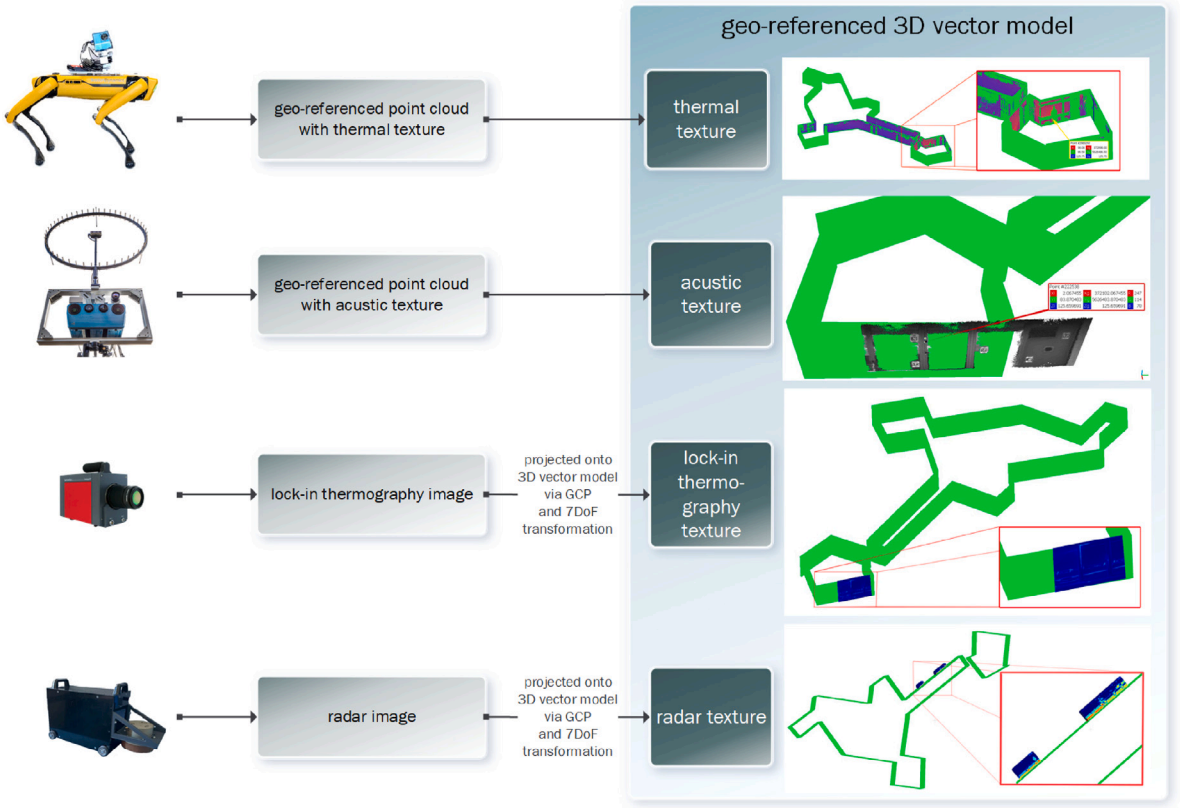

Fig. 13. Overview of data processing workflow integrating measurement results in the geo-referenced 3D vector model.

helps to understand the observed scene's temperature distribution. Fig. 15(a) shows a 3D point cloud, partially with recorded and plotted colour-coded IR data, and the trajectory as light blue points. Fig. 15(b) shows only the points with temperature information and the trajectory for better visualization with an additional rendering filter. These indoor IR measurements were carried out (at an ambient temperature of 20 °C) mainly to demonstrate the sensor combination of IPS and its integrated IR camera and were not further evaluated.

Finally, the IPS 3D thermal cloud, or respectively points closest to the façades, were projected into the 3D vector model using the least squares method (Fig. 16).

4.1.2. Acoustic measurements

Integration of acoustic measurements with point cloud model

The acoustic sensor captures RGB images along with corresponding 2D acoustic measurements, which are represented as colour-coded acoustic images, as shown in Figs. 17(a), 17(c) and 17(e). In principle, if data from an external sensor in the form of suitable image data is available, this sensor information can be directly mapped to the generated 3D points using the same method described for thermal data in Section 4.1.1. Therefore, achieving accurate spatial registration between the external sensor and the IPS stereo

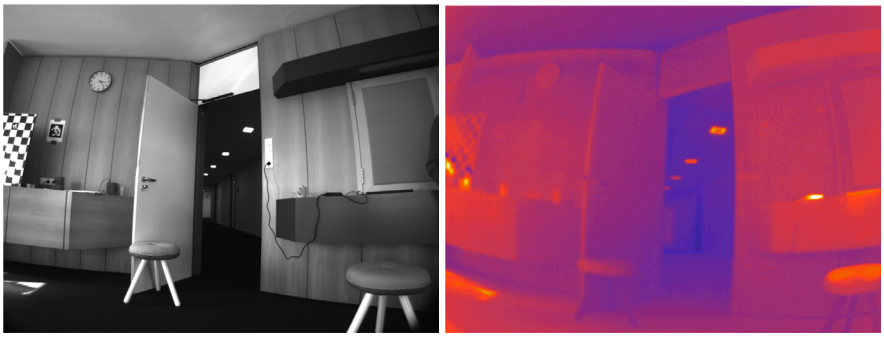

(a) (b)

Fig. 14. Simultaneously recorded images of the IPS-IR system (a) Left IPS RGB image; (b) IR image. (For interpretation of the references to colour in this figure legend, the reader is referred to the web version of this article.)

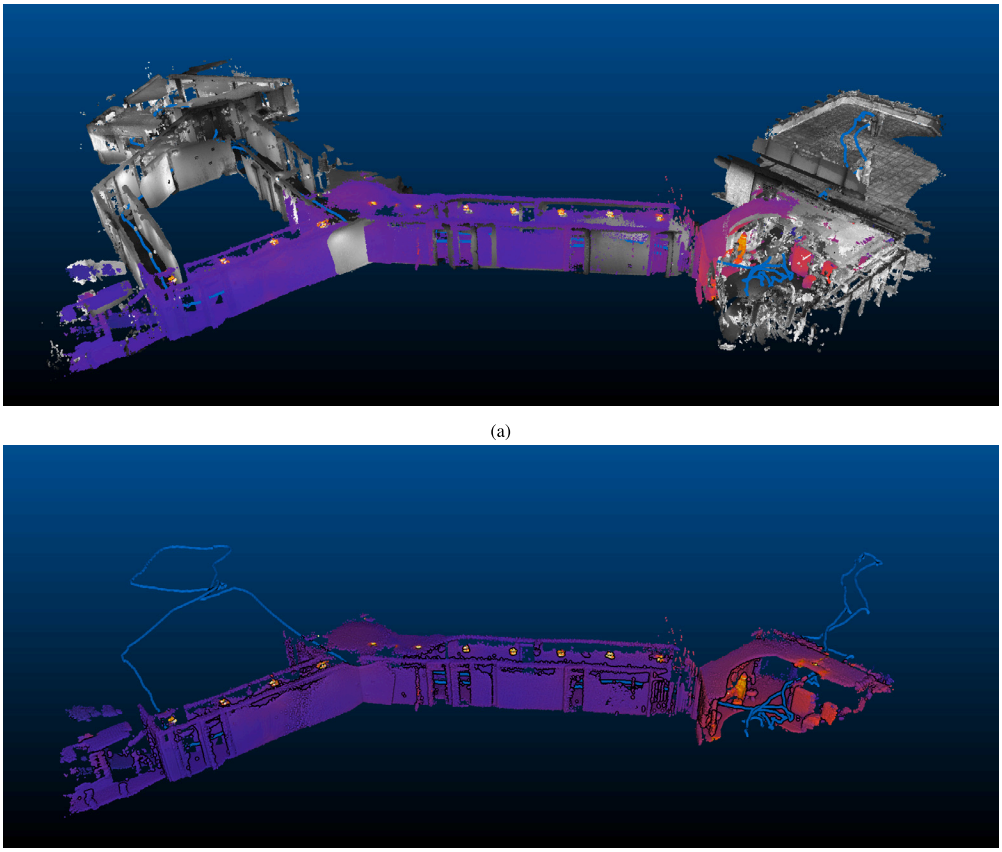

(a)

(b)

Fig. 15. Evaluation results obtained from the IPS measurements with the integrated IR camera (a) 3D point cloud, partial with recorded and plotted colour-coded IR data; (b) All 3D points with given temperature information and the IPS trajectory, rendered with an additional filter. (For interpretation of the references to colour in this figure legend, the reader is referred to the web version of this article.)

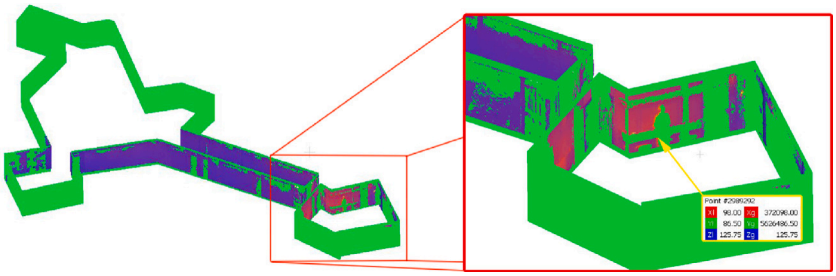

Fig. 16. Localization of IPS-IR evaluation results by projection of the IPS 3D thermal cloud onto the 3D vector model; absolute coordinates of the marked thermal point in UTM are [372 098.00, 5 626 486.50, 125.75] [m].

camera is crucial. The registration process between the acoustic camera and the IPS determines the relative orientation between the RGB camera of the acoustic camera and the IPS. It is essential to ensure reliable registration between the acoustic sensor and the RGB camera within the acoustic camera system. The evaluated dataset consists of IPS stereo images and acoustic measurements captured from fixed viewpoints. Figs. 17(b), 17(d) and 17(f) depict local 3D point clouds generated from IPS stereo pairs taken at a fixed viewpoint, with mapped acoustic information evaluated for different third-octave centre frequencies: 1.6 kHz (Figs. 17(a) and 17(b)), 4 kHz (Figs. 17(c) and 17(d)), and 20 kHz (Figs. 17(e) and 17(f)). Due to the complex measurement setup and time-consuming process, IPS navigation data were not recorded between the acoustic measurements at different locations. As a result, in this campaign, the mapping of acoustic images was performed for single, local IPS 3D point clouds, and the colour-coded point clouds had to be manually referenced with the overall cloud, as described in the next subsection.

Integration of acoustic measurements within 3D vector model

The acoustic measurements, once integrated within the IPS 3D point cloud model, were transformed into the UTM WGS84 coordinate system using the Helmert transformation and the georeferenced IPS point cloud. Additionally, the acoustic measurements were projected onto the 3D vector model using the least squares method (Fig. 18). The absolute XY position of the measurements was compared to Apple Maps data. The coordinates of the measured acoustic spot in the model were determined as [372 102.06 m E, 5 626 483.83 m N]. The absolute position of this spot measured in Apple Maps was found to be [7.18599°E, 50.77596°N], equivalent to [372 101.85 m E, 5 626 483.33 m N] in the UTM coordinate system. The difference between the two positions is minimal, with only a few centimetres, which is within the limits of measurement uncertainty. To validate the relative position of the acoustic measurements, the distance to the window frame was measured in the model and compared to the on-site distance. The deviation between the two measurements was found to be 1.2 cm.

4.1.3. Lock-in thermography

Since the measurement using lock-in thermography was conducted with a separate IR camera, the resulting lock-in images were manually integrated into the 3D model. This integration involved rectifying and georeferencing the lock-in thermography image using the georeferenced IPS 3D point cloud. Finally, the image was projected onto the 3D vector model, as depicted in Fig. 19. By comparing this image with the results obtained from the acoustic method (Fig. 17), the leak in the top left corner of the door is once again visible.

This integration process ensures that the lock-in thermography results are aligned with the spatial information captured by the IPS and incorporated into the comprehensive 3D model. The manual integration allows for a direct visual comparison between the results of lock-in thermography and other measurement techniques, facilitating a holistic understanding of the building's condition.

4.1.4. Tracer gas

To semi-automatically illustrate the spatial concentration of hydrogen, a tracer gas measuring device along with an IPS was attached to the SPOT so, that the relative positions of the two devices were known. The idea was to synchronize the IPS time measurement with the tracer gas time measurement on the beginning of the SPOT run by setting tracer gas time corresponding to an unique IPS button trigger event. As the tracer gas meter did not accept time settings, the possible time assignment was too imprecise and visualization of the hydrogen spreading measurements was inaccurate.

4.1.5. Radar

For radar data acquisition, local measurements were conducted, capturing the start point and end point of each acquisition. Leveraging the IPS 3D point cloud and 3D vector model, the radar images of wall cross-sections were semi-automatically rectified and georeferenced. This process ensured accurate alignment of the radar data with the spatial information captured by the IPS and incorporated into the comprehensive 3D model. Fig. 20 illustrates the position of the radar data within the 3D vector model, providing a visual representation of the integration of radar measurements.

By incorporating radar data into the database, information on the internal structures of the walls can be included in the model. The semi-automated rectification and georeferencing of radar images ensure their accurate positioning within the 3D model, enabling effective visualization and analysis of the structural characteristics of the building.

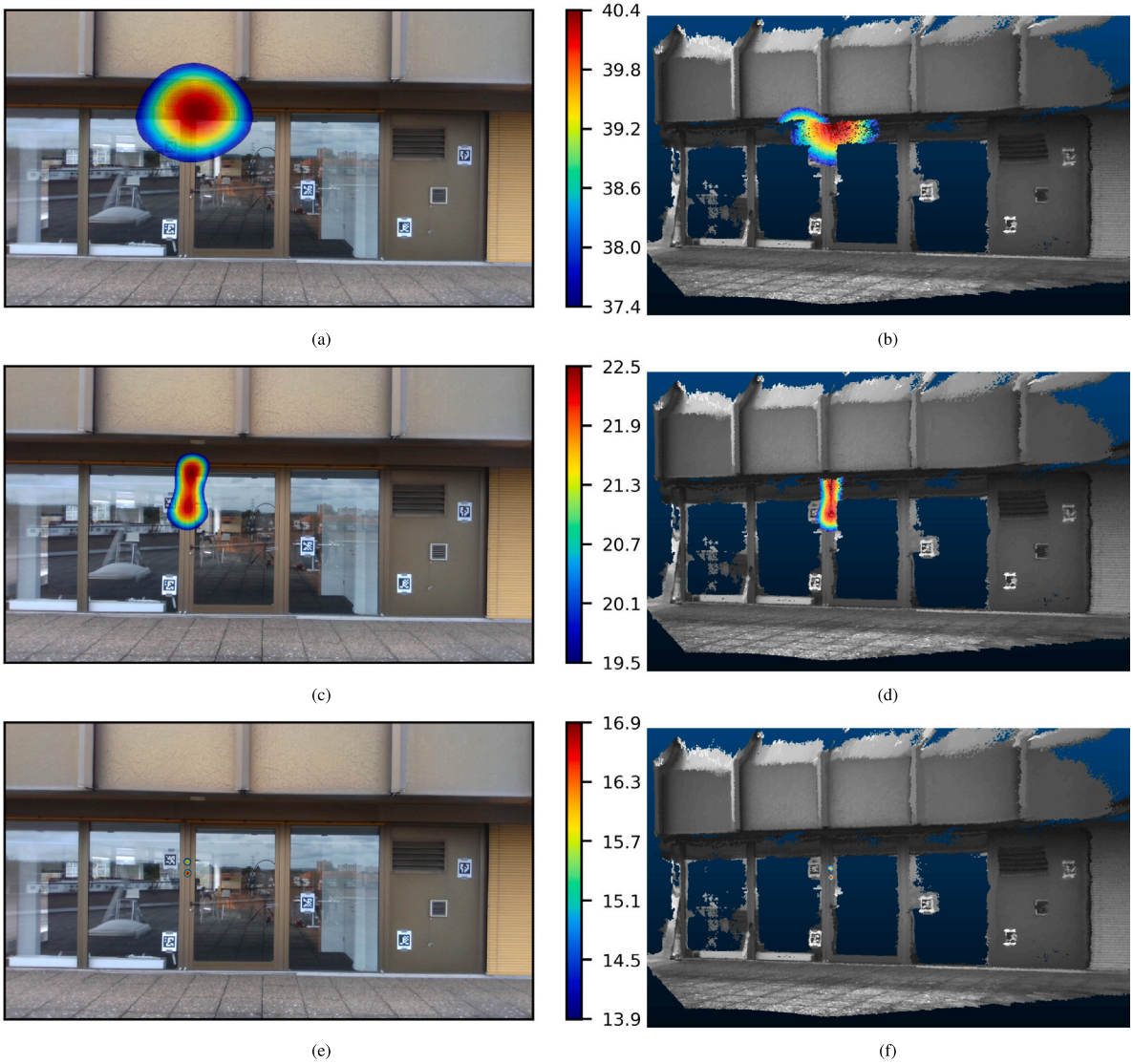

Fig. 17. Acoustic results of the acoustic camera (left) and their integration into 3D IPS point cloud (right): superimposed sound pressure levels are shown in dB and selected third-octave frequency bands with centre frequencies of 1.6 kHz (top), 4 kHz (middle) and 20 kHz (bottom). (For interpretation of the references to colour in this figure legend, the reader is referred to the web version of this article.)

Fig. 18. Acoustic measurements projected onto a 3D vector model given in UTM coordinates (the height is ellipsoidal) and visualized in Apple Maps.

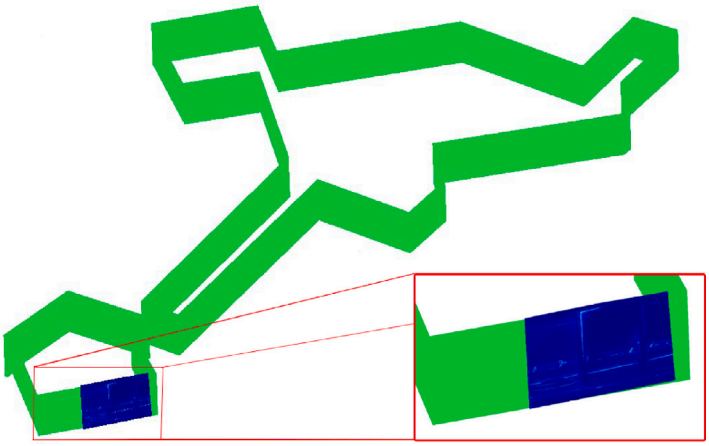

Fig. 19. Image of lock-in measurement integrated into 3D model. The absolute position of the leak in the top left corner of the door in UTM is [372 102.06, 5 626 483.77, 126.43][m].

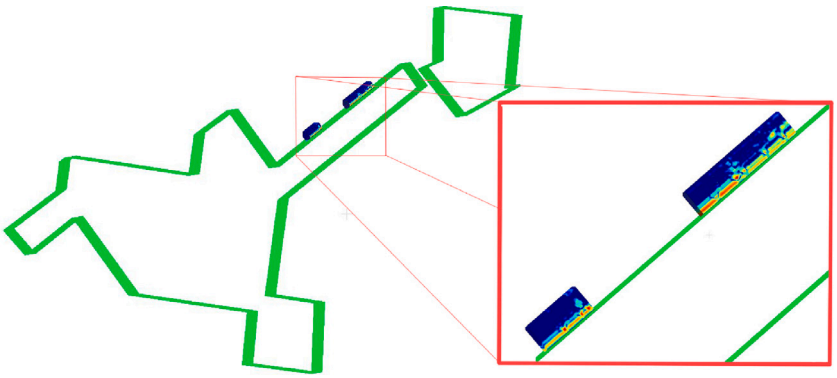

Fig. 20. Image of radar measurement integrated into 3D model. The absolute position of the radar data in UTM is: from start point [372 091.54, 5 626 497.00, 125] to end point [372 092.32, 5 626 496.03, 125] and from start point [372 094.15, 5 626 493.75, 125] to end point [372 095.71, 5 626 491.80, 125][m].

5. Conclusion and outlook

The results of the measurement campaign show how the outcome of various inspection techniques can be combined and represented in a joint framework if they are carefully spatially referenced. By integrating the outcome of different measurements, it becomes possible to create a comprehensive 3D model of the inspected rooms, incorporating visualizations of the results from various measurements modalities. The innovation of our approach lies in its ability to consolidate different data sources into a joined analysis platform.

The individual measurements provide mostly structural information about the building. The visual data collected with the IPS enables the generation of a point cloud, which can be further processed into a polygon model of the building parts. The thermal IR layer provides insights into the homogeneity of the building structure, highlighting variations in building materials or their thickness that affect heat flows through walls, floors, and ceilings. These show up as small temperature differences on the surface and, therefore, different intensity – or colour – in the thermography images. The radar measurements provide additional information about the structure of these building elements as its radiation penetrates the materials. Therefore, it allows to clearly distinguish between changes in thickness or changes in material and can resolve several layers of different materials or objects. The acoustic transmission and lock-in thermography measurements complement the structural analysis by identifying small openings in the building envelope or between rooms, which can significantly impact air exchange and energy efficiency. These combined measurements cover a significant range of structural properties and provide a comprehensive understanding of the building's characteristics. The measurement results themselves can be visualized in a 3D model as shown in Section 4.

The structural building information obtained through our measurement methods serves several purposes. The knowledge about geometry, air exchange paths, and composition of the building components can support safety and security measures by providing insights into evacuation routes, smoke spreading paths, and the presence of flammable materials. Additionally, this information is valuable for energy performance assessment and the preparation of energetic retrofit measures. Understanding the air exchange paths and the composition of building components is one of the key factors for evaluating heat loss and heat conduction through

the building envelope, both of which have a significant impact on energy efficiency. This depends on the thickness and composition of materials in the envelope components. The geometry of the building is another key information for heating demand calculations as the heated volume and the area of external surfaces can be derived from it. All of this information – either completely or parts of it – can be obtained by the measurements presented in this paper.

Some of the measurements were performed using a mobile robotic platform as carrier of the sensors. Ongoing research focuses on further developing the mobility and autonomy of the sensor system aiming to improve measurement efficiency and reduce dependency on human labour. These advancements hold the potential for significantly faster inspections and increased automation in the future. The focus of this study was on demonstrating an integrated building analysis approach and novel measurement methodologies. All preparations, measurements, their evaluation, and integration into the BIM were carried out by experienced specialists closely involved in the development of the measurement and evaluation techniques. While interaction and integration of systems were demonstrated, complete automation remains a work in progress. Presently, operation, data evaluation, interpretation, and integration into the BIM necessitate skilled personnel, making its usage labour-intensive and relatively costly. A favourable cost–benefit ratio is likely attainable primarily for special buildings, such as large historical buildings or those with complex hidden structures.

Future work will focus on developing a workflow to efficiently translate these measurements into BIM-compatible formats, with the objective of further automating and streamlining the process. Additionally, there will be a focus on expanding the capabilities of our measurement techniques for integration within digital twin technologies. Furthermore, development efforts are required to quantitatively correlate measurement results with performance indicators, such as thermal transmittance (U-value) and air exchange rate.

In conclusion, the integration of multiple measurement techniques and their visualization within a unified 3D model enables a comprehensive understanding of the structural, energetic, and safety-related properties of buildings. Continued research and development in this field will contribute to more efficient and automated measurement processes, further enhancing our ability to evaluate and optimize building performance.

CRediT authorship contribution statement

Nicole Janotte: Writing – review & editing, Writing – original draft, Project administration, Investigation, Conceptualization. **Benedikt Kölsch:** Writing – review & editing, Writing – original draft, Methodology, Investigation. **Eckhard Lüpfert:** Writing – original draft, Investigation. **Johannes Pernpeintner:** Writing – original draft, Methodology, Investigation. **Björn Schiricke:** Writing – original draft, Project administration, Investigation, Funding acquisition, Conceptualization. **Jacob Estevam Schmiedt:** Writing – review & editing, Project administration, Funding acquisition, Conceptualization. **Dirk Baumbach:** Writing – original draft, Investigation. **André Choinowski:** Writing – original draft, Investigation, Data curation. **Dennis Dahlke:** Writing – original draft, Formal analysis, Data curation. **Ines Ernst:** Writing – original draft, Formal analysis, Data curation. **Magdalena Linkiewicz:** Writing – original draft, Visualization, Formal analysis, Data curation. **Adrian Schischmanow:** Writing – original draft, Supervision, Investigation. **Stephan Dill:** Writing – original draft, Investigation. **Tobias Karrer:** Investigation, Formal analysis. **Markus Peichl:** Writing – original draft, Supervision, Methodology. **David Heuskin:** Writing – original draft, Investigation.

Declaration of competing interest

The authors declare the following financial interests/personal relationships which may be considered as potential competing interests: Pernpeintner has patent #10 2022 102 824 (German Patent Number) issued to Johannes Pernpeintner, Benedikt Kölsch, Eckhard Lüpfert. If there are other authors, they declare that they have no known competing financial interests or personal relationships that could have appeared to influence the work reported in this paper.

Data availability

The data that has been used is confidential.

Acknowledgements

The authors acknowledge the support of the entire team at the DLR Institute for the Protection of Terrestrial Infrastructures for providing the test site and collaboration through the duration of the project. Special thanks are extended to Daniel Schallowetz, Marco Berger, and Christof Hammer for their valuable contributions in the implementation and operation of SPOT.

References

[1] T. Czerniawski, F. Leite, Automated digital modeling of existing buildings: A review of visiual object recognition methods, Autom. Constr. (2020) http://dx.doi.org/10.1016/j.aucon.2020.103131.

[2] T. Czerniawski, F. Leite, Automated segmentation of RGB-D images into a comprehensive set of buiding components using deep learning, Adv. Eng. Inform. (2020) http://dx.doi.org/10.1016/j.aei.2020.101131.

[3] F. Xue, L. Wu, W. Lu, Semantic enrichment of Building and City Information Models: a ten-year review, Adv. Eng. Inform. (2021) http://dx.doi.org/10.1016/j.aei.2020.101245.

[4] I. Poza-Casado, A. Meiss, M.Á. Padilla-Marcos, J. Feijó-Muñoz, Airtightness and energy impact of air infiltration in residential buildings in Spain, Int. J. Vent. 20 (3–4) (2021) 258–264, http://dx.doi.org/10.1080/14733315.2020.1777029.

[5] N. Hurel, V. Leprince, VIP 46: Building airtightness impact on Energy Performance (EP) calculations, AIVC Vent. Inf. Pap. (2023).

[6] W. Tan, C. Li, K. Wang, G. Zhu, Y. Wang, L. Liu, Dispersion of carbon dioxide plume in street canyons, Process Saf. Environ. Prot. 116 (2018) 235–242, http://dx.doi.org/10.1016/j.psep.2018.01.020.

[7] D. Deaves, Dense gas dispersion modelling, J. Loss Prev. Process Ind. 5 (4) (1992) 219–227, http://dx.doi.org/10.1016/0950-4230(92)80044-9.

[8] P. Shrestha, J.W. DeGraw, M. Zhang, X. Liu, Multizonal modeling of SARS-CoV-2 aerosol dispersion in a virtual office building, Build. Environ. 206 (2021) 108347, http://dx.doi.org/10.1016/j.buildenv.2021.108347.

[9] T. Lim, J. Cho, B.S. Kim, The predictions of infection risk of indoor airborne transmission of diseases in high-rise hospitals: Tracer gas simulation, Energy Build. 42 (8) (2010) 1172–1181, http://dx.doi.org/10.1016/j.enbuild.2010.02.008.

[10] A. Börner, D. Baumbach, M. Buder, A. Choinowski, I. Ernst, E. Funk, D. Grießbach, A. Schischmanow, J. Wohlfeil, S. Zuev, IPS – a vision aided navigation system, Adv. Opt. Technol. 6 (2) (2017) 121–129, http://dx.doi.org/10.1515/aot-2016-0067.

[11] D. Grießbach, D. Baumbach, S. Zuev, Stereo-vision-aided inertial navigation for unknown indoor and outdoor environments, in: 2014 International Conference on Indoor Positioning and Indoor Navigation, IPIN, 2014, pp. 709–716, http://dx.doi.org/10.1109/IPIN.2014.7275548.

[12] A. Schischmanow, D. Dahlke, D. Baumbach, I. Ernst, M. Linkiewicz, Seamless navigation, 3D reconstruction, thermographic and semantic mapping for building inspection, Sensors 22 (13) (2022) http://dx.doi.org/10.3390/s22134745.

[13] J. Wohlfeil, D. Grießbach, I. Ernst, D. Baumbach, D. Dahlke, Automatic camera system calibration with a chessboard enabling full image coverage, in: The International Annals of the Photogrammetry, Remote Sensing and Spatial Information Sciences, in Print, 2019.

[14] A. Choinowski, D. Dahlke, I. Ernst, S. Pless, I. Rettig, Automatic calibration and co-registration for a stereo camera system and a thermal imaging sensor using a chessboard, in: ISPRS Geospatial Week 2019, 2019,

[15] E. Olson, AprilTag: A robust and flexible visual fiducial system, in: Proceedings of the IEEE International Conference on Robotics and Automation (ICRA), IEEE, 2011, pp. 3400–3407.

[16] G. Bradski, The OpenCV library, Dr. Dobb's J. Softw. Tools (2000).

[17] MathWorks®, Landmark SLAM using AprilTag markers, 2022, URL https://de.mathworks.com/help/nav/ug/landmark-slam-using-apriltag-markers. (Accessed 29 August 2022).

[18] I. Ernst, H. Hirschmüller, Mutual information based semi-global stereo matching on the GPU, in: Advances in Visual Computing, in: Lecture Notes in Computer Science, Vol. 5358, Springer Berlin Heidelberg, Berlin, Heidelberg, 2008, pp. 228–239, http://dx.doi.org/10.1007/978-3-540-89639-5_22.

[19] H. Hirschmüller, D. Scharstein, Evaluation of stereo matching costs on images with radiometric differences, IEEE Trans. Pattern Anal. Mach. Intell. 31 (9) (2009) 1582–1599.

[20] R.B. Rusu, S. Cousins, 3D is here: Point cloud library (PCL), in: (ICRA) International Conference on Robotics and Automation, 2011, pp. 1–4, http://dx.doi.org/10.1109/ICRA.2011.5980567.

[21] CloudCompare, GPL software, 2019, URL http://www.cloudcompare.org/.

[22] D. Frommholz, M. Linkiewicz, A.-M. Poznanska, Inlining 3D reconstruction, multi-source texture mapping and semantic analysis using oblique aerial imagery, in: XXIII ISPRS Congress, Technical Commission III, XLI (B3), Copernicus Publications, 2016, pp. 605–612, http://dx.doi.org/10.5194/isprsarchives-XLI-B3-605-2016.

[23] D. Frommholz, M. Linkiewicz, H. Meißner, D. Dahlke, Reconstructing buildings with discontinuities and roof overhangs from oblique aerial imagery, Int. Arch. Photogramm. Remote Sens. Spat. Inf. Sci. - ISPRS Arch. XLII-1 (2017) 465–471.

[24] M. Prignon, G. Van Moeseke, Factors influencing airtightness and airtightness predictive models: A literature review, Energy Build. 146 (2017) 87–97, http://dx.doi.org/10.1016/j.enbuild.2017.04.062.

[25] M.H. Sherman, W.R. Chan, Building air tightness: Research and practice, in: Building Ventilation: The State of the Art, Earthscan, London, 2006, pp. 137–162.

[26] C. Banister, M. Bartko, J. Berquist, I. Macdonald, M. Vuotari, A. Wills, Energy and emissions effects of airtightness for six non-residential buildings in Canada with comparison to contemporary limits and assumptions, J. Build. Eng. 58 (2022) 104977, http://dx.doi.org/10.1016/j.jobe.2022.104977.

[27] L. Kempton, D. Daly, G. Kokogiannakis, M. Dewsbury, A rapid review of the impact of increasing airtightness on indoor air quality, J. Build. Eng. 57 (2022) 104798, http://dx.doi.org/10.1016/j.jobe.2022.104798, URL https://linkinghub.elsevier.com/retrieve/pii/S2352710222008117.

[28] I.S. Walker, D.J. Wilson, Field validation of algebraic equations for stack and wind driven air infiltration calculations, HVAC&R Res. 4 (2) (1998) 119–139, http://dx.doi.org/10.1080/10789669.1998.10391395.

[29] ASTM International, E1186-17: Air leakage site detection in building envelopes and air barrier systems, 2017.

[30] D.N. Keast, Acoustic location of infiltration openings in buildings: Final report, 1978.

[31] G. Benedetto, E. Brosio, A relation between transmission loss and air infiltration characteristics in windows, 1981.

[32] T. Sonoda, F. Peterson, A sonic method for building air-leakage measurements, Appl. Energy 22 (3) (1986) 205–224, http://dx.doi.org/10.1016/0306-2619(86)90003-6.

[33] M. Ringger, P. Hartmann, Evaluation of an acoustical method for detecting air leaks, Air Infiltration Rev. 11 (1) (1989) 6–9.

[34] O.A. Hassan, An alternative method for evaluating the air tightness of building components, Build. Environ. 67 (2013) 82–86, http://dx.doi.org/10.1016/j.buildenv.2013.05.007.

[35] B. Kölsch, B. Schiricke, J. Estevam Schmiedt, B. Hoffschmidt, Estimation of air leakage sizes in building envelope using high-frequency acoustic impulse response technique, in: Proceedings of the 40th AIVC - 8th TightVent - 6th Venticool Conference, Air Infiltration and Ventilation Centre, 2019.

[36] B. Kölsch, I.S. Walker, W.W. Delp, B. Schiricke, B. Hoffschmidt, Comparison of airflow and acoustic measurements for evaluation of building air leakage paths in a laboratory test apparatus, in: Proceedings of the 41st AIVC - ASHRAE IAQ Joint Conference, American Society of Heating, Refrigeration and Air Conditioning Engineers, Inc., 2021.

[37] V. Iordache, T. Catalina, Acoustic approach for building air permeability estimation, Build. Environ. 57 (2012) 18–27, http://dx.doi.org/10.1016/j.buildenv.2012.04.008.

[38] K. Varshney, J.E. Rosa, I. Shapiro, D. Scott, Air-infiltration measurements in buildings using sound transmission loss through small apertures, Int. J. Green Energy 10 (5) (2013) 482–493, http://dx.doi.org/10.1080/15435075.2012.675603.

[39] U. Berardi, S. Pouyan, Exploring acoustical approaches for pre-screening the airtightness of building enclosures, in: Proceedings of the 177th Meeting of the Acoustical Society of America, 2019.

[40] B. Kölsch, I.S. Walker, B. Schiricke, W.W. Delp, B. Hoffschmidt, Quantification of air leakage paths: a comparison of airflow and acoustic measurements, Int. J. Vent. 22 (2021) 101–121, http://dx.doi.org/10.1080/14733315.2021.1966576.
[41] O. Jaeckel, Strengths and weaknesses of calculating beamforming in the time domain, in: Gesellschaft zur Förderung Angewandter Informatik (Ed.), Proceedings of the BeBeC, 8th Berlin Beamforming Conference, 2006.
[42] H. Teutsch, Modal Array Signal Processing: Principles and Application of Acoustic Wavefield Decomposition, in: Lecture Notes in Control and Information Sciences, Vol. 348, Springer, Berlin Heidelberg, 2007.
[43] B. Kölsch, B. Schiricke, E. Lüpfert, B. Hoffschmidt, Detection of air leakage in building envelopes using microphone arrays, in: Proceedings of the 41st AIVC - ASHRAE IAQ Joint Conference, American Society of Heating, Refrigeration and Air Conditioning Engineers, Inc., 2022.
[44] B. Kölsch, Investigation of an Improved Acoustical Method for Determining Airtightness of Building Envelopes (Dissertation), RWTH Aachen University, Düren, 2022, p. 190, http://dx.doi.org/10.2370/9783844085839.
[45] B. Schiricke, M. Diel, B. Kölsch, Field testing of an acoustic method for locating air leakages in building envelopes, Buildings 14 (4) (2024) http://dx.doi.org/10.3390/buildings14041159.
[46] International Organization for Standardization, ISO 9972:2015: Thermal performance of buildings - Determination of air permeability of buildings - Fan pressurization method, 2015.
[47] ASTM International, E779-19: Standard test method for determining air leakage rate by fan pressurization, 2019.
[48] A. Mélois, F. Carrié, M. El Mankibi, B. Moujalled, Uncertainty in building fan pressurization tests: Review and gaps in research, J. Build. Eng. 52 (2022) 104455, http://dx.doi.org/10.1016/j.jobe.2022.104455.
[49] F.R. Carrié, V. Leprince, Uncertainties in building pressurisation tests due to steady wind, Energy Build. 116 (2016) 656–665, http://dx.doi.org/10.1016/j.enbuild.2016.01.029.
[50] T. Kalamees, Air tightness and air leakages of new lightweight single-family detached houses in Estonia, Build. Environ. 42 (6) (2007) 2369–2377, http://dx.doi.org/10.1016/j.buildenv.2006.06.001.
[51] BlowerDoor GmbH, Bau.tools BlowerDoor, 2018, URL https://www.blowerdoor.com/measurement-systems/bautools.
[52] O. Breitenstein, W. Warta, M.C. Schubert, Lock-in Thermography: Basics and Use for Evaluating Electronic Devices and Materials, third ed., in: Springer Series in Advanced Microelectronics, Vol. 10, Springer-Verlag, Berlin, Heidelberg, 2018, http://dx.doi.org/10.1007/978-3-319-99825-1.
[53] C.A. Stutt, Low-frequency spectrum of lock-in amplifiers, 1949.
[54] B. Kölsch, J. Pernpeintner, B. Schiricke, E. Lüpfert, Air leakage detection in building façades by combining lock-in thermography with blower excitation, Int. J. Vent. (2023) http://dx.doi.org/10.1080/14733315.2023.2198791.
[55] X. Liu, Z. Peng, X. Liu, R. Zhou, Dispersion characteristics of hazardous gas and exposure risk assessment in a multiroom building environment, Int. J. Environ. Res. Public Health 17 (1) (2020) 199, http://dx.doi.org/10.3390/ijerph17010199.
[56] D. Mu, C. Shu, N. Gao, T. Zhu, Wind tunnel tests of inter-flat pollutant transmission characteristics in a rectangular multi-storey residential building, part B: Effect of source location, Build. Environ. 114 (2017) 281–292, http://dx.doi.org/10.1016/j.buildenv.2016.12.031.
[57] MALA GPR Australia, [Link], 2021, URL https://www.malagpr.com.au/.
[58] Leica Geosystems AG, [Link], 2023, URL https://leica-geosystems.com/.
[59] GSSI Geophysical Survey Systems, Inc, [Link], 2023, URL https://www.geophysical.com/.
[60] D.J. Daniels, A review of GPR for landmine detection, Sens. Imaging 7 (3) (2006) 90.
[61] O.L.L. Tellez, B. Scheers, Ground-penetrating radar for close-in mine detection, Mine Action Res. Exp. R. Milit. Acad. Belg. (2017).
[62] A. Heinzel, M. Schartel, R. Burr, R. Bähnemann, E. Schreiber, M. Peichl, C. Waldschmidt, A comparison of ground-based and airborne SAR systems for the detection of landmines, UXO, and IEDs, in: Radar Sensor Technology XXIII, vol. 11003, SPIE, 2019, pp. 9–17.
[63] ImpulseRadar Sweden AB, [Link], 2023, URL https://impulseradargpr.com/road-bridge-inspection/.
[64] M.O.F. Howlader, T.P. Sattar, S. Dudley, Development of a wall climbing robotic ground penetrating radar system for inspection of vertical concrete structures, Int. J. Mech. Mechatronics Eng. 10 (8) (2016) 1382–1388.
[65] Infraspect, [Link], 2023, URL https://infraspect.com/ground-penetrating-radar/.
[66] T. Zheng, Z. Chen, J. Luo, L. Ke, C. Zhao, Y. Yang, SiWa: see into walls via deep UWB radar, in: Proceedings of the 27th Annual International Conference on Mobile Computing and Networking, 2021, pp. 323–336.
[67] A. Haas, M. Peichl, S. Dill, Layer determination of buidling structures with SAR in near field environment, in: 2019 16th European Radar Conference (EuRAD), IEEE, 2019, pp. 209–212.
[68] J. Estevam Schmiedt, Gtom – Messsystem für Schnelle Und Genaue Energetische Analysen von Gebäudehüllen für Gebäude und Quartiere, Final Report 03ET1405A, Deutsches Zentrum für Luft- und Raumfahrt e.V., 2020.
[69] P. Gorzalka, A. Haas, G. Golubeva, J. Estevam Schmiedt, M. Peichl, B. Hoffschmidt, Material investigations to facilitate the applicability of microwave radar to energy-related wall structure analysis, Mater. Struct. 54 (3) (2021) 1–12.